I&EC research
Industrial & Engineering Chemistry Research
pubs.acs.org/IECR
Article

Data-Driven Reduced-Order Model for Bubbling Fluidized Beds

Published as part of Industrial & Engineering Chemistry Research virtual special issue "Multiscale Modeling and Artificial Intelligence for Multiphase Flow Science".

Xiaofei Li, Shuai Wang, Dali Kong, Kun Luo,* and Jianren Fan

Cite This: Ind. Eng. Chem. Res. 2024, 63, 1634−1648

Read Online

ACCESS | Metrics & More | Article Recommendations | Supporting Information

ABSTRACT: Simulation of dense gas−solid flow in fluidized beds is a computationally intensive procedure, and emerging speedup simulation methods are still unsatisfactory. This work developed a pioneering data-driven reduced-order model (ROM) for efficient modeling of dense gas−solid flow in bubbling fluidized beds (BFB) by integrating the proper orthogonal decomposition (POD) and the radial basis function neural network (RBFNN). Specifically, this study extracts the fundamental eigenvectors of the gas−solid flow process and constructs a prediction function for the corresponding eigenvector coefficients. The effectiveness of this ROM is conclusively assessed by comparing it with the full-order model (FOM) in terms of simulated results and performance criteria. The results indicate that the 10-bases-ROM and 64-bases-ROM exhibit 50 and 90% of the energy, respectively, and achieve flow field reconstruction accuracy of 50 and 90%. Moreover, compared to the FOM, the 10-bases-ROM and the 64-bases-ROM demonstrate 700-fold and 120-fold increases in simulation efficiency, respectively. These findings indicate that the proposed model has the potential to be an effective tool for industrial engineering process predictions in real time.

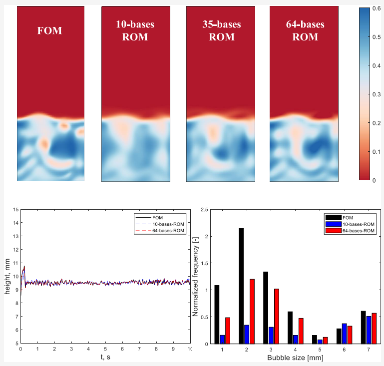

1. INTRODUCTION

Nowadays, the exacerbating climate change and the exhaustion of fossil fuel reserves present significant obstacles to the progress of human civilization. Consequently, the fluidized bed reactor, which is an effective and energy-conserving energy utilization system, has gained increasing interest due to its superior gas−solid interaction efficiency, exceptional heat and mass transfer properties, and minimal pollution emission.[1,2] The fluidized bed is a highly intricate multiphase reaction system in which a large number of extremely complex physical and chemical processes occur, involving nonlinear coupling of mass, momentum, and energy between phases.[3]

With advancements in computer technology, numerical simulation has gained widespread acceptance and has become an essential tool in fluidized bed studies, which provides a highly efficient and cost-effective way to gain insights into the gas−solid flow, temperature, and gas component distributions in fluidized beds.[4−6] Several simulation methods have been developed, including the Euler−Euler method and the Euler−Lagrangian method. Of these methods, the two-fluid method (TFM) in the Euler−Euler framework is widely utilized in numerical simulations of fluidized beds. The TFM simulation has been proven to be computationally efficient. However, the high-fidelity full-order model (FOM) of the TFM simulation still demands substantial computational resources due to the requirement of a tiny time step to accurately resolve each iteration of the discretized governing equations. As a result, the FOM is inadequate to meet the industry's real-time response demands.[7]

Currently, data-driven reduced-order model (ROM) approaches have shown great potential for efficient and accurate modeling of high-dimensional nonlinear systems. This method relies on basis projections to effectively decrease the effective degrees of freedom in the original system, thus reducing the computational cost of high-fidelity simulations. By constructing a low-dimensional and parsimonious dynamical system from existing data, the ROM can considerably reduce the complexity of the original system, ultimately resulting in improved computational efficiency.[8] At present, many ROMs have been proposed, among which proper orthogonal decomposition (POD) is the most representative.[7,9−12] POD originated from the statistical analysis of vector data and has been widely used in data dimensionality reduction, flow field analysis, and other application scenarios.[13] The research on POD-based ROM represents a new and popular trend in utilizing hybrid machine learning methods to reduce the complexity of the network structure and flow. In terms of portability, this method is applicable to various flows, making it a universal approach.[14]

Received: October 24, 2023
Revised: December 12, 2023
Accepted: December 25, 2023
Published: January 12, 2024

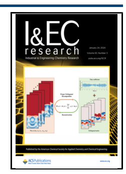

https://doi.org/10.1021/acs.iecr.3c03747
Ind. Eng. Chem. Res. 2024, 63, 1634−1648

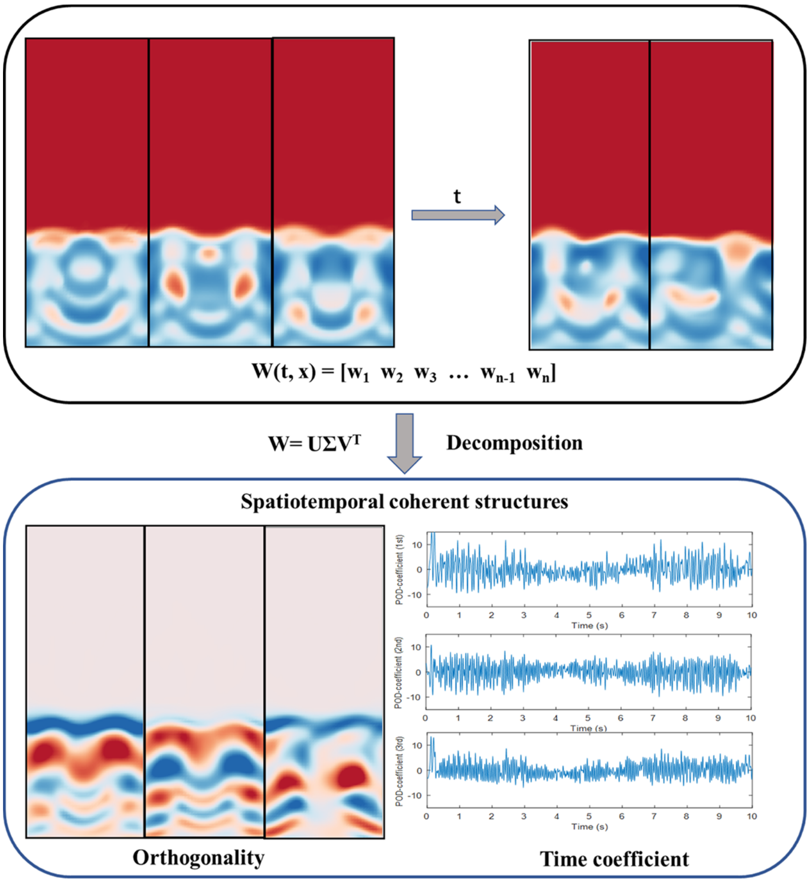

Figure 1. Illustration of modal decomposition of a dense gas–solid flow.

The POD-based ROM can be divided into an intrusive ROM[15] and a nonintrusive ROM. The intrusive ROM approach involves solving the governing equations and projecting them into a subspace comprising proper orthogonal basis vectors to derive ordinary differential equations. Although this approach

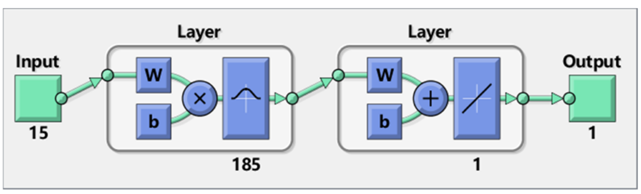

Figure 2. RBF neural network structure.

boasts a more mathematically rigorous form and stronger generalization ability, it may not be conducive to code reproduction and could lack stability. In contrast, the nonintrusive ROM approach establishes a surrogate model between the input and output data, extracts the appropriate orthogonal basis vectors from a snapshot, obtains the POD coefficients using the surrogate model, and constructs the ROM by interpolating the hypersurface. Surrogate models encompass a variety of models, including Kriging models, radial basis functions (RBF), neural networks, and others. Specifically, the Kriging model is an unbiased estimation model that utilizes known test point data to predict the response of unknown test points. The principle of the RBF is to utilize the superposition of a series of kernel functions to fit the original function. As a powerful tool, the neural network has been widely used in

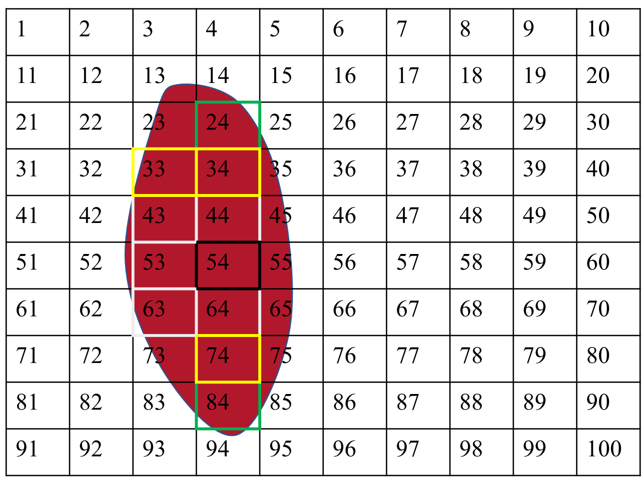

$\mathbf{Cell}_{\mathbf{bub}}$ = [24, 33, 34, 43, 44, 53, 54, 63, 64, 74, 84]
$\mathbf{Cell}_{\mathbf{target}}$ = $\mathbf{Bub}_{\mathbf{initial}}$ = [54]
$\mathbf{Bub}_{\mathbf{1st\ search}}$ = [43, 44, 53, 63, 64]
$\mathbf{Bub}_{\mathbf{2nd\ search}}$ = [33, 34, 74]
$\mathbf{Bub}_{\mathbf{3rd\ search}}$ = [24, 84]

Figure 3. Schematic representation of the bubble search algorithm.

modeling gas–solid flow. Zhu et al.[16,17] pioneeringly used traditional and artificial neural network (ANN) data-driven modeling (DDM) methods to derive a variety of models, including the mesoscale drag model, heat transfer model, and reaction model in filtered gas–solid flow with big data from high-resolution simulations. Compared with traditional corre-

https://doi.org/10.1021/acs.iecr.3c03747
Ind. Eng. Chem. Res. 2024, 63, 1634–1648

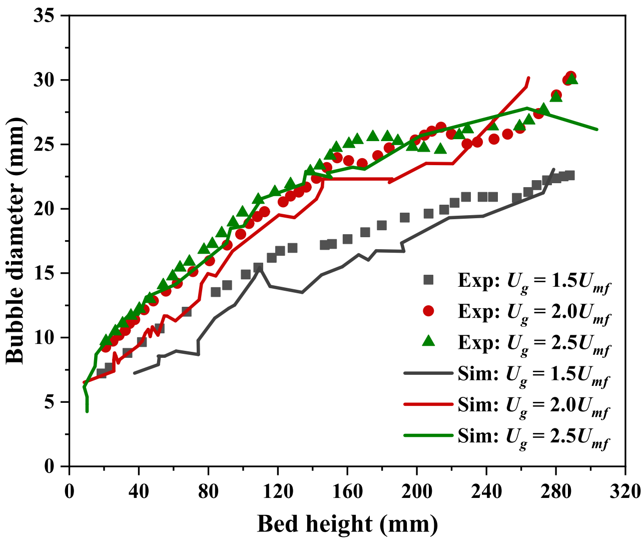

Figure 4. Comparison of the predicted bubble diameter with the experimental data.[34]

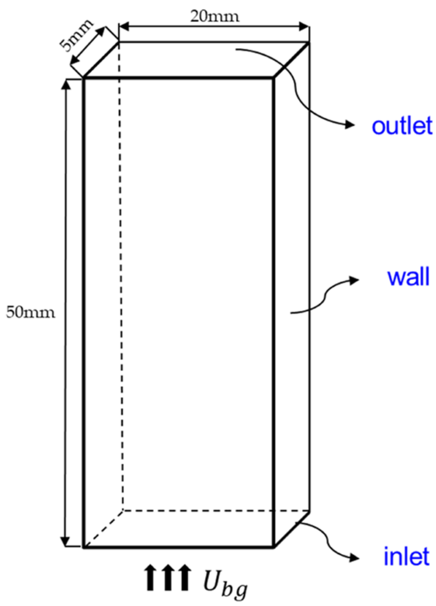

Figure 5. Schematic diagram of the BFB.

Table 1. Simulation Settings of the Validation

parameters	value
geometry configuration, $x \times y \times z$	20 mm × 5 mm × 50 mm
computational grids, $N_x \times N_y \times N_z$	40 × 10 × 100
material quality, m	2.145 g, 2.681 g
fluid velocity, U_{bg}	0.10 m/s, 0.18 m/s
time step, Δt	5×10^{-4} s

Table 2. Cases Studied in This Work

	case-1 (base case)	case-2	case-3
initial bed material quality	2.145 g	2.145 g	2.681 g
inlet velocity	0.10 m/s	0.18 m/s	0.18 m/s

lation prediction, DDM exhibits higher accuracy. The results also demonstrate that the coarse-grid simulations combined with ANN agree well with experiment measurements.

Table 3. Physical Properties Used in the Simulations

Gas Phase		
viscosity	Pa·s	1.8×10^{-5}
density	kg/m^3	1.0
Solid Phase		
density	kg/m^3	2.5×10^3
diameter	mm	0.16
frictional viscosity	kg/(m·s)	0.3
restitution coefficient		0.9
virtual mass coefficient		0.5
packing limit		0.63

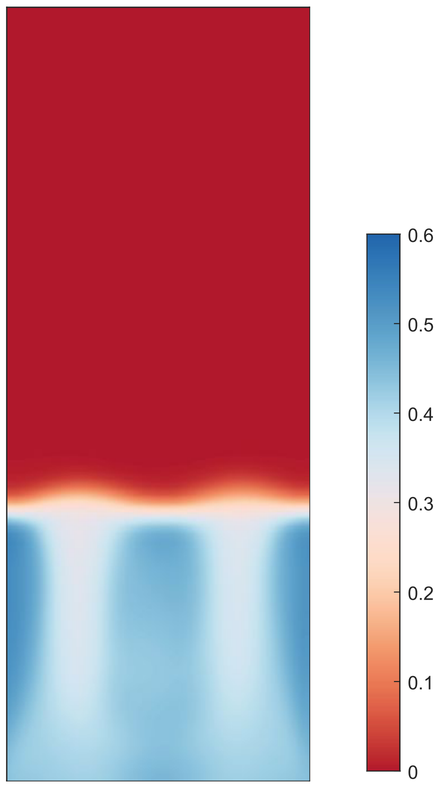

Figure 6. Time-averaged solid holdup distribution obtained from the POD base.

By adopting this approach, a more efficient and stable method of constructing ROMs can be achieved.[9] The nonintrusive model approach offers several advantages, such as code reusability, ease of transplantation, high cohesion, low coupling, relative stability, a simple structure, and higher computational efficiency. Due to these benefits, the present study adopts a nonintrusive approach to construct the ROM.

Currently, several researchers have conducted extensive research on ROMs. In terms of the nonintrusive ROM, some researchers have combined the POD method with RBF and Kriging methods and have applied it to various fields such as heat conduction, natural convection, phase change heat storage, aerothermodynamics of hypersonic vehicles, and computational fluid dynamics (CFD) analysis of wind loads for photovoltaic systems.[18−22] Other researchers have focused on uncertainty quantification in CFD, proposing a surrogate model based on POD-Kriging to quantify uncertainty in the dynamical system.[23−25] Additionally, compressive sensing extracted from the coarse-grid covariance matrix has been combined with this method to achieve greater efficiency.[25] Lee et al.[26] combined

https://doi.org/10.1021/acs.iecr.3c03747
Ind. Eng. Chem. Res. 2024, 63, 1634−1648

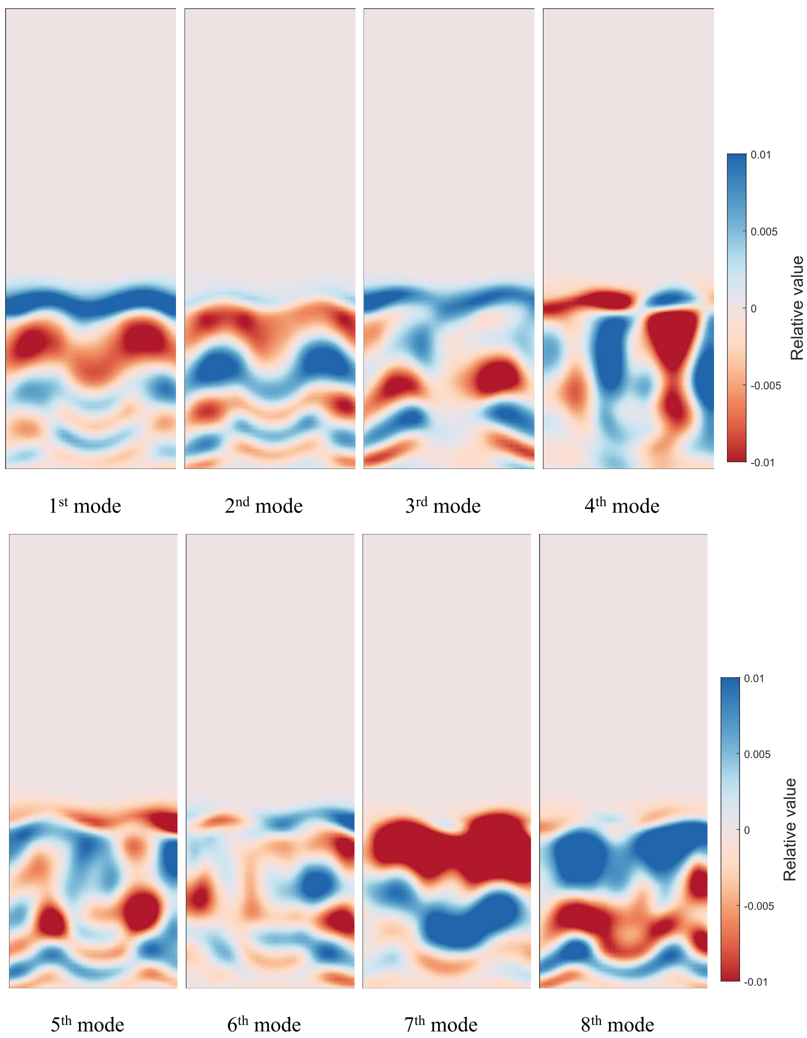

Figure 7. Solid holdup of the first 8 orders of POD bases.

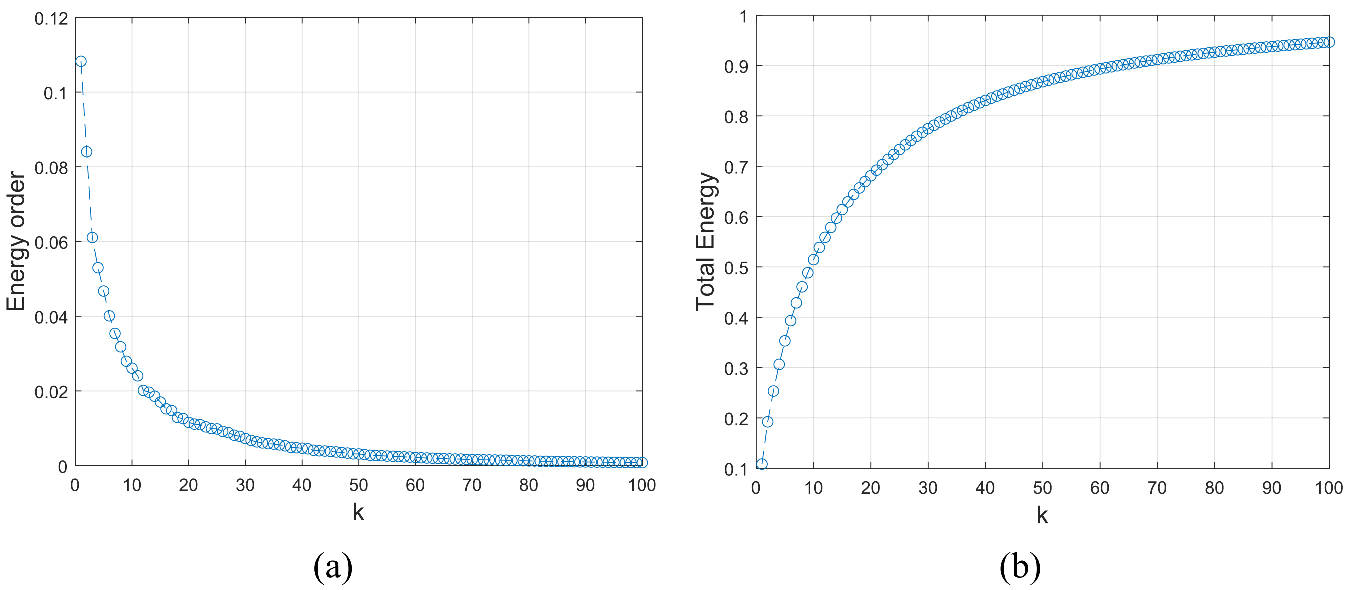

Figure 8. (a) First one hundred orders of energy sorting; (b) cumulative modal energy for the first k orders (k from 1 to 100).

POD with the Kriging/RBF method to develop a nonintrusive ROM of a 500 MW four-corner tangential pulverized coal boiler, which simplified the three-dimensional (3D) furnace to a two-dimensional (2D) plane and reproduced the total amount of secondary air and the 3D distribution of combustion stoichiometric ratios in the organ region. Li et al.[27] adopted a

https://doi.org/10.1021/acs.iecr.3c03747
Ind. Eng. Chem. Res. 2024, 63, 1634−1648

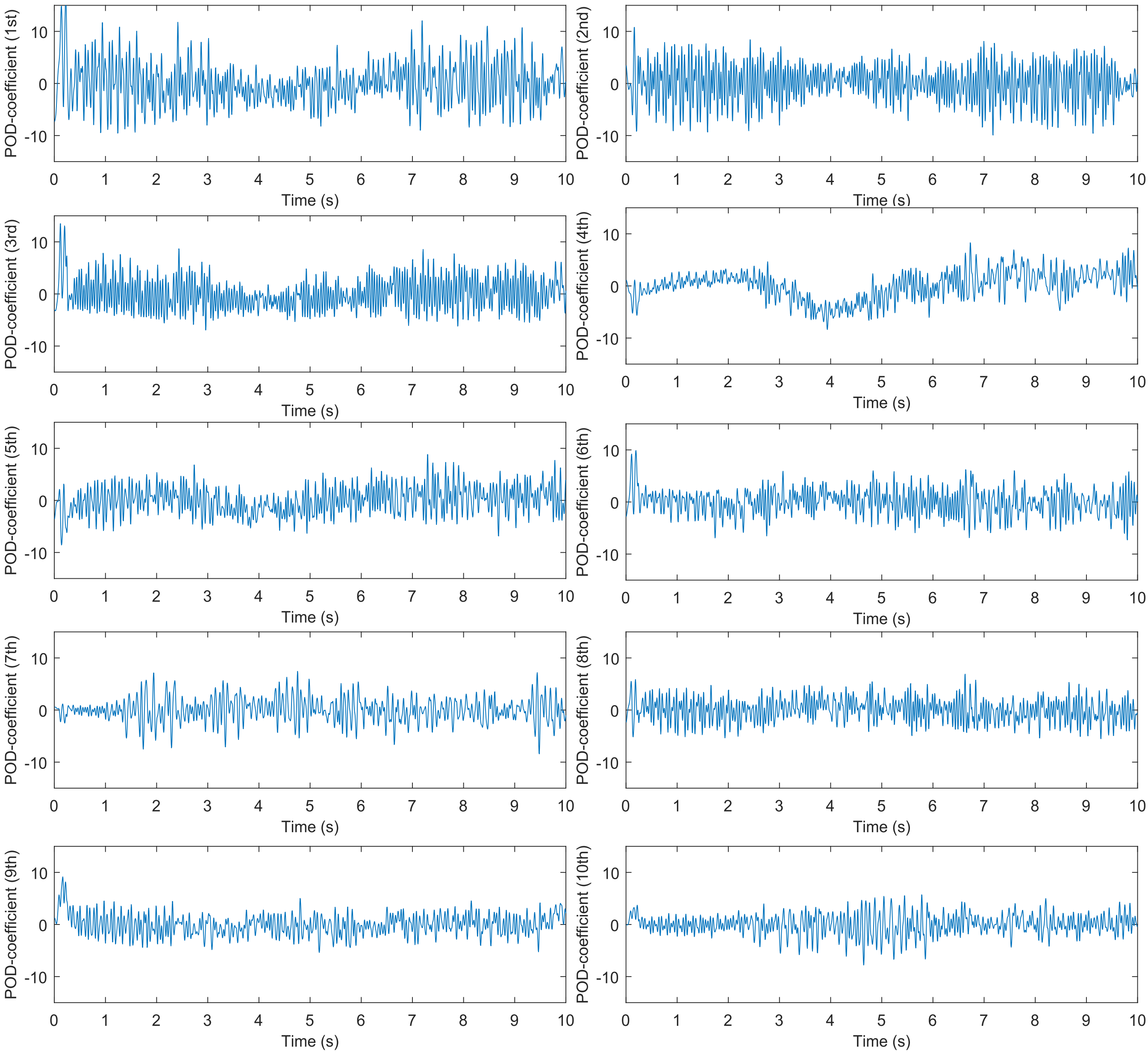

Figure 9. Time-evolution profiles of the coefficients of POD bases.

POD method based on the Lanczos algorithm to efficiently generate a set of POD basis vectors. After projecting the numerical snapshot into the simplified space constructed by the POD basis vectors, the RBF was used to construct a series of multidimensional functions of POD coefficients, thus developing a nonintrusive ROM for large-scale Euler−Lagrangian simulations, overcoming the huge computational cost problem caused by the CFD-DEM method, and effectively reproducing the gas−solid flow in a bubbling fluidized bed (BFB).

However, current literature indicates a dearth of online real-time predictive ROM that caters to fluidized beds. Moreover, there are few reports on ROMs tailored for fluidized beds. Hence, this study's innovation lies in the construction of an innovative ROM utilizing the POD/RBFNN method, enabling the real-time prediction of gas−solid flow and its primary characteristics in the BFB. Critical parameters in the BFB, including bed expansion height, bubble distribution, and others, are predicted in real time. The ROM combined with actual data is suitable for application in a digital twin setting, which consists of physical products, virtual products, and data connections. The results of this study exhibit good agreement with those computed by the TFM. Single-step prediction and multistep prediction are adopted for online ROM, respectively. Single-step prediction exhibits exceptional accuracy in short-term prediction, whereas multistep prediction is more efficient. This paper utilizes a bubble search algorithm to efficiently and precisely characterize bubbles in the BFB reactor. The algorithm facilitates the acquisition of plentiful physical−thermal−chemical properties of the bubbles.[28] Moreover, this study showcases the computational efficiency superiority of the developed ROMs. The proposed ROMs enable online real-time prediction, offering significant guidance for industrial production processes.

The paper is organized as follows. Section 2 outlines the mathematical approach to the ROM and bubble search algorithm. Section 3 presents the numerical setup for the BFB.

https://doi.org/10.1021/acs.iecr.3c03747
Ind. Eng. Chem. Res. 2024, 63, 1634−1648

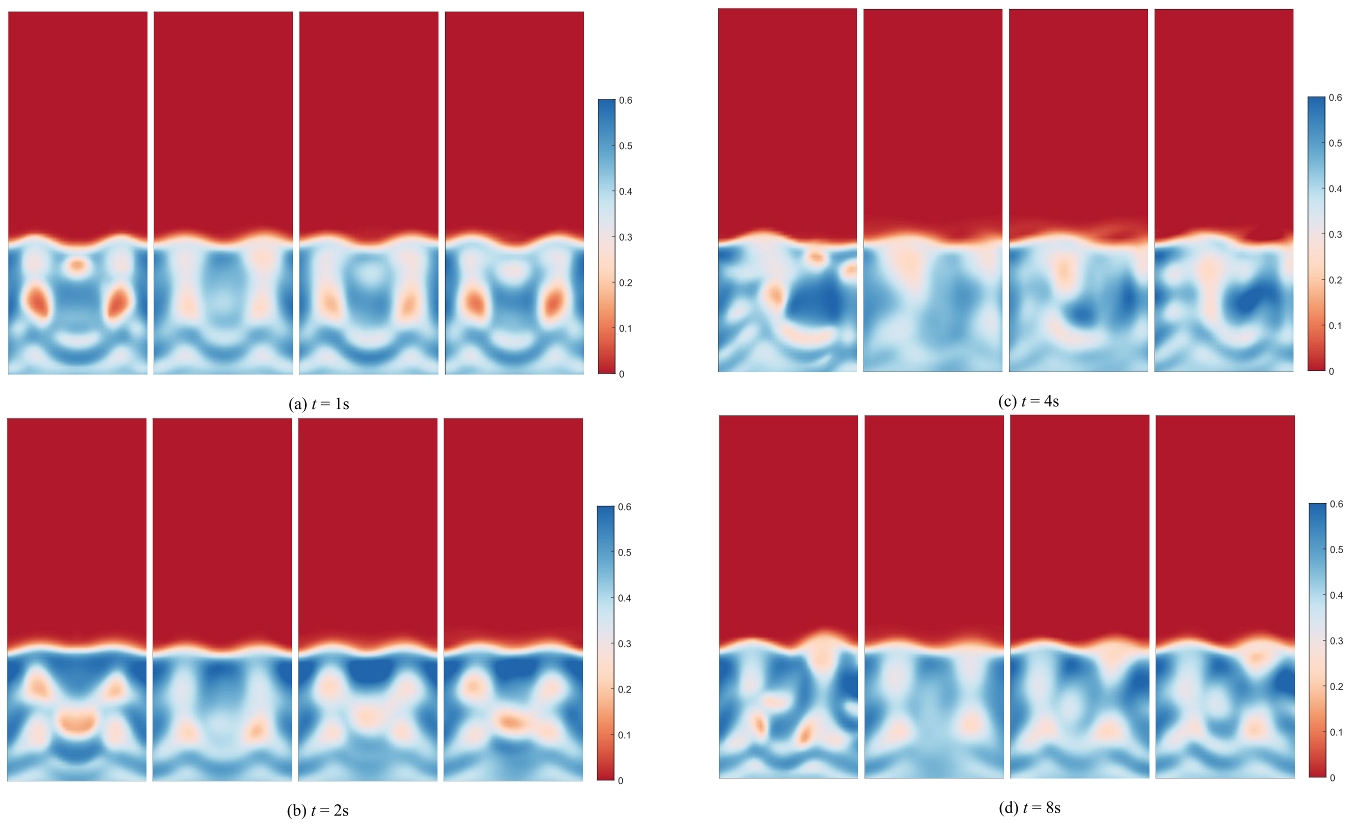

Figure 10. Solid holdup distributions at different time instants: (a) $t = 1$s; (b) $t = 2$s; (c) $t = 4$s; (d) $t = 8$s; (from left to right: FOM,10-bases-ROM,35-bases-ROM, and 64-bases-ROM).

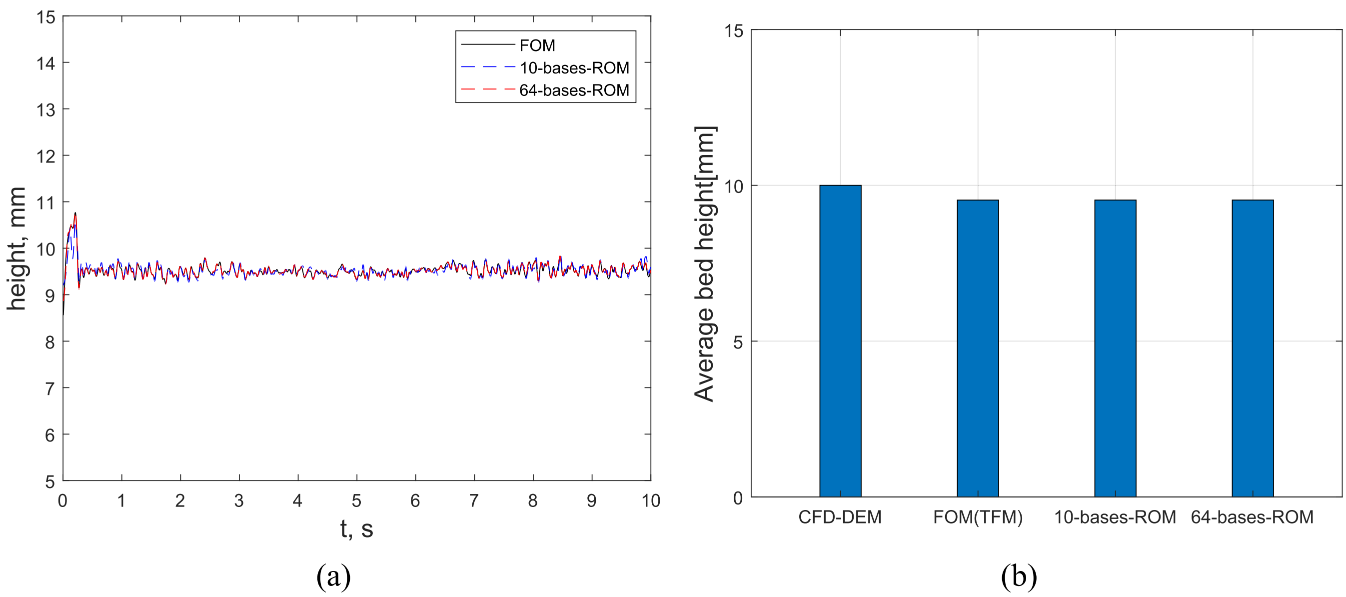

Figure 11. Bed expansion height in the BFB predicted by the FOM and single-step ROM in Case-1: (a) time-evolution bed expansion height; (b) time-averaged bed expansion height.

In Section 4.1, POD mode decomposition is described. Subsequently, Sections 4.2 and 4.3 provide the reconstruction accuracy for various orders of ROM and compare the accuracy difference between single-step prediction and multistep prediction. Furthermore, Section 4.4 quantifies the time reduction achieved by different-order ROMs. The conclusions and future developments are presented in the final section.

2. METHODOLOGY

The formulation of the CFD-DEM and TFM methods employed is briefly reviewed in Section 2.1. The basic ideas and specific calculation processes of the data-driven method are summarized in Section 2.2. A novel bubble search algorithm is presented in Section 2.3 for bubble characterization.

2.1. CFD-DEM and TFM Methods.

The mainstream methods for numerical simulation of dense gas–solid systems are the CFD-DEM and TFM methods. In the former method, the movement of each solid particle is tracked individually in the Lagrangian framework using Newton's second law. In the latter method, the solid particle is assumed to be a continuous phase and is described by solving the volume-averaged Navier−Stokes equations. The CFD-DEM and TFM methods have been widely applied in various chemical engineering processes. The main equations involved are outlined in Tables S1 and S2 of the Supporting Information.

2.2. Data-Driven Methods. The data-driven method used in this work combines proper orthogonal decomposition (POD) and a radial basis function neural network (RBFNN), which is a low-dimensional approximation of high-dimensional flow fields. POD modes reconstruct a data set by extracting the dominant eigenvectors based on Frobenius norm optimality, with the modes ranked in terms of energy content. RBFNN is used to predict the selected POD mode coefficients. Combining the decomposed POD coefficients with RBFNN, the ROM of the flow field can be obtained. This ROM exhibits robust stability, enabling highly stable predictions within its corresponding mode coefficients without the concerns of divergence. The algorithm is summarized in Figure 1, which shows the spatio-temporal coherent structures with different characteristics obtained by processing the same series of time snapshots with POD. The specific formulation of the POD and RBFNN will be presented in Sections 2.2.1 and 2.2.2.

2.2.1. Proper Orthogonal Decomposition (POD). The POD method calculates the eigenvalues and eigenvectors of the FOM matrix to extract the dominant features of the original flow field. These features are sorted in descending order based on their corresponding eigenvalues, which indicate the number of features contained in the corresponding eigenvectors. A finite number of eigenvectors are then chosen to form the POD basis, which encapsulates most of the information on the flow field, enabling the decomposition of the flow field to be accomplished.

At each time step, every snapshot of the target variable (voidage) is taken from the FOM and is used to construct a matrix ($\mathbf{W}$, $M \times N$) according to the distribution of voidage in space and time, where M is the number of grids and N is the number of snapshots in the full-order simulation. The POD method uses only a limited number of basis functions to construct a ROM, with the number of basis vectors $k \leq \min\{M, N\}$. In general, the number of grids in the simulation is much larger than the number of snapshots on the time scale, i.e., $M \gg N$. Therefore, k is less than N in most ROMs. Through the linear combination of k basis vectors, a solution is obtained whose dimension is much smaller than that of the original data set.

POD construction steps are as follows:

First, the matrix $\mathbf{W}$ obtained is time-averaged and decentralized, and the time-averaged operation is

$$W_0(x) = \left[\frac{1}{M}\sum_{i=1}^{M} W_i^j(x)\right]_{(1\times N)} \tag{1}$$

where $W_i^{\,j}(x)$ is the target variable value of each grid (i) at the time (j), M is the number of grids, and N is the number of snapshots in the full-order simulation.

Decentralization:

$$\{x_1, x_2, ..., x_n\} = \{w_1 - W_0, w_2 - W_0, ..., w_n - W_0\} \tag{2}$$

where $\boldsymbol{w}_i$ is the original data and $\boldsymbol{x}_i$ is the data after decentralization.

To ensure that the vector $\boldsymbol{\Phi}_\mathbf{i}$ can contain most of the energy and features after projection, it is necessary to minimize the distance from the data $\boldsymbol{x}_i$ to the projection vector $\boldsymbol{\Phi}_\mathbf{i}$, i.e., to maximize the following formula:

$$\frac{1}{n}\sum_{i}^{n} |x_i \cdot \boldsymbol{\Phi}_i| \tag{3}$$

where $|\boldsymbol{x}_i \cdot \boldsymbol{\Phi}_\mathbf{i}|$ is the inner product of the vector $\boldsymbol{x}_i$ and the vector $\boldsymbol{\Phi}_\mathbf{i}$, which is equivalent to

$$\frac{1}{n}\| X^T \boldsymbol{\Phi}_i \|_2^2 = \frac{1}{n}(X^T\boldsymbol{\Phi}_i)^T(X^T\boldsymbol{\Phi}_i) = \frac{1}{n}\boldsymbol{\Phi}_i^T X X^T \boldsymbol{\Phi}_i \tag{4}$$

where $\mathbf{X} = [x_1, x_2, x_3, \cdots, x_n]$, $\mathbf{XX}^\mathbf{T}$ is a positive semidefinite matrix (eigenvalue greater than or equal to 0).

In this work, the singular value decomposition method (SVD) is used to solve the maximum value of eqs 3 and 4. As a realization of the proper orthogonal decomposition method, SVD has a wide range of applications. SVD compresses a large matrix into the form of multiplication of several small matrices and can decompose any form of a matrix, so there is always a singular value decomposition for any form of matrix $\mathbf{A}$: $\mathbf{A} = \mathbf{U}\sum\mathbf{V}^\mathbf{T}$. The matrix sizes of $\mathbf{A}$, $\mathbf{U}$, $\sum$, and $\mathbf{V}^\mathbf{T}$ are $(M \times N)$, $(M \times M)$, $(M \times N)$, and $(N \times N)$, respectively. Among them, the orthogonal vector in $\mathbf{U}$ is called the left singular vector; the elements in $\sum$ except the diagonal are all 0, and the elements on the diagonal are called singular values; the orthogonal vector in $\mathbf{V}$ is called the right singular vector. In general, the values of $\sum$ are given in descending order.

Therefore, the reduced order basis can be obtained as follows:

$$\frac{\| X^T \boldsymbol{\Phi}_k \|}{\| \boldsymbol{\Phi}_k \|} \leq \sigma_k(X^T) \tag{5}$$

where $\sigma_k(\boldsymbol{X}^\mathbf{T})$ is the singular value of $\mathbf{X}^\mathbf{T}$ (i.e., the square root of the eigenvalue λ_k of $\mathbf{XX}^\mathbf{T}$) and $\boldsymbol{\Phi}_k$ is the corresponding eigenvector. The singular value is the largest at $k = 1$. According to the maximization principle in eq 4, it can be obtained that the eigenvector of $\boldsymbol{\Phi}_1$ contains the most features, and $\boldsymbol{\Phi}_2$ is the eigenvector containing the most energy after $\boldsymbol{\Phi}_1$. The eigenvalues and corresponding eigenvectors are obtained in turn, and the reduced order basis is obtained.

The energy proportion of the first k order reduced basis is

$$I(k) = \frac{\sum_{i=1}^{k}\lambda_i}{\sum_{i=1}^{N}\lambda_i} \tag{6}$$

Therefore, depending on the required accuracy, the original flow field can be restored by selecting an appropriate orthogonal basis.

In a transient fluidized bed process, the results are predicted based on the extracted orthogonal basis vectors:

$$\hat{W}(x, t) = W_0(x) + \sum_{k=1}^{N_{\mathrm{POD}}} \alpha_k(t)\cdot\boldsymbol{\Phi}_k(x) \tag{7}$$

where $\alpha_k(t)$ is a coefficient that varies with time in transient fluidized bed simulation. $\boldsymbol{\Phi}_k(\boldsymbol{x})$ is the orthogonal basis selected by SVD decomposition. Assuming that the energy contained in the N_{POD} orthogonal bases meets the requirements, by multiplying and summing the first N_{POD} orthogonal bases and coefficients, most of the features in the FOM are obtained, and then the target variable is predicted.

https://doi.org/10.1021/acs.iecr.3c03747
Ind. Eng. Chem. Res. 2024, 63, 1634−1648

2.2.2. Radial Basis Function Neural Network (RBFNN). RBFNN is widely used in time series forecasting. Compared with deep machine learning, such as long short-term neural networks, RBFNN has a faster training speed, is easier to train, and does not require a sufficient training data set. These characteristics are very important in a real digital twin system, which requires the ability to quickly build predictive models. Compared with polynomials, RBFNN has better performance in degrees of freedom and accuracy. Hence, in this paper, RBFNN is selected as the coefficient prediction method. The RBFNN contains a hidden radial basis layer and a output linear layer. In this paper, The Gaussian kernel function is selected as the RBF in the hidden layers, the number of which depends on the actual needs of the problem. Nonlinear data in low-dimensional space are transformed into linear separable data in high-dimensional space. The output layers are obtained through the linear mapping of the hidden layer, which means the output is the linear weighted sum of the hidden layer neural units.

As the base in hidden layers, the RBF is a scalar function that exhibits radial symmetry. It is typically defined as a monotonic function of the radial distance, often expressed in terms of the Euclidean distance between a given sample and the center of the data. By utilizing the RBF, it becomes possible to obtain the coefficients of the corresponding POD bases at a specific target time, based on the coefficient values of a certain POD basis at a known time. Consequently, it becomes feasible to predict the time series through this process. To elaborate on this further, the single-step resolution process can be described as follows:

$$\begin{aligned}\alpha_k^n &= f_k(\boldsymbol{\alpha}_k^{\text{input}}) \\ &= f_k([\alpha_k^{n-i}]),\ k \in \{1, 2, \cdots, N_{\text{POD}}\},\ i \\ &\quad \in \{1, 2, \cdots, N_{\text{input}}\}\end{aligned} \tag{8}$$

where α_k^n is the coefficient of the kth POD basis at time n. α_k^{n-i} is the POD basis coefficient vector at the $(n-i)$ time. N_{POD} and N_{input} are the number of POD bases and RBFNN inputs, respectively.

RBF can be regarded as a linear combination of a set of scalar functions and corresponding weighting coefficients:

$$f_k(\boldsymbol{\alpha}_k^{\text{input}}) = \sum_{j=1}^{N_{\text{RBF}}} \omega_k(j) * \phi(\| \boldsymbol{\alpha}_k^{\text{input}} - \hat{\boldsymbol{\alpha}}(\boldsymbol{j}) \|) \tag{9}$$

where $\phi(\|\boldsymbol{\alpha}_k^{\text{input}} - \hat{\boldsymbol{\alpha}}(j)\|)$ is the kernel function, which represents the function value related to the L^2 norm between the known point and the predicted point; $\omega_k(j)$ is the desired RBF weight coefficient. Assuming that N_{RBF} is the number of known interpolation nodes,

$$\{\hat{\boldsymbol{\alpha}}(j), f(\hat{\boldsymbol{\alpha}}(j))\}|_{j=1}^{N_{\text{RBF}}} \tag{10}$$

where $f(\hat{\boldsymbol{\alpha}}(j))$ is the value corresponding to $\hat{\boldsymbol{\alpha}}(j)$.

Then, eq 9 can be transformed into (the subscript k is dropped for convenience):

$$\begin{bmatrix} \phi_{11} & \phi_{12} & \cdots & \phi_{1N_{\text{RBF}}} \\ \phi_{21} & \phi_{22} & \cdots & \phi_{2N_{\text{RBF}}} \\ \vdots & \vdots & \ddots & \vdots \\ \phi_{N_{\text{RBF}}1} & \phi_{N_{\text{RBF}}2} & \cdots & \phi_{N_{\text{RBF}}N_{\text{RBF}}} \end{bmatrix} \begin{bmatrix} \omega_1 \\ \omega_2 \\ \vdots \\ \omega_{N_{\text{RBF}}} \end{bmatrix} = \begin{bmatrix} f_k(\boldsymbol{\alpha}_k^{\text{input}}(1)) \\ f_k(\boldsymbol{\alpha}_k^{\text{input}}(2)) \\ \vdots \\ f_k(\boldsymbol{\alpha}_k^{\text{input}}(N_{\text{RBF}})) \end{bmatrix} \tag{11}$$

where (if the Gaussian kernel function is adopted):

$$\phi_{ij} = \phi(\| \boldsymbol{\alpha}_k^{\text{input}} - \hat{\boldsymbol{\alpha}}(j) \|) = \exp\left(-\frac{\| \boldsymbol{\alpha}_k^{\text{input}} - \hat{\boldsymbol{\alpha}}(j) \|^2}{2\sigma^2} \right) \tag{12}$$

$\boldsymbol{\Phi} = [\phi_{ij}]$ is the interpolation matrix, and eq 11 can be simplified as

$$\boldsymbol{\Phi W} = A \tag{13}$$

Substitute eqs 10 into 13 to obtain the RBF weight coefficient value. Substituting the weight coefficient into eqs 8 and 9, the POD coefficient value $\alpha_k(t_n)$ at time t_n can be obtained.

As mentioned above, the data of the next single step is predicted based on the ability to obtain actual data in time, which is called a single-step prediction. A multistep prediction is required if a more extended period needs to be predicted. The multistep prediction is given in eq 14:

$$\begin{aligned}\boldsymbol{\alpha}_k^{\text{output}} &= [\alpha_k^{n+l}] = f_k(\boldsymbol{\alpha}_k^{\text{input}}) = f_k([\alpha_k^{n-i}]),\ k \\ &\quad \in \{1, 2, \cdots, N_{\text{POD}}\},\ i \in \{1, 2, \cdots, N_{\text{input}}\},\ l \\ &\quad \in \{1, 2, \cdots, N_{\text{output}}\}\end{aligned} \tag{14}$$

where N_{output} is the number of RBFNN outputs.

As shown in Figure 2, this RBFNN predicts a POD coefficient at an unknown time through the known POD coefficients in 15 time steps. The RBFNN contains two layers. The first layer is the hidden radial basis layer, which uses the radial basis function to calculate the weighted input. The number of neurons is 185, which is consistent with the number of training samples. The second layer is the output linear layer, which is used to calculate the output of the network. Both layers have a bias b. The RBFNN is constructed by MATLAB. To avoid overfitting, the propagation spread of the RBF needs to be regulated. The choice of spread value affects the diffusion degree of the model, consequently impacting its complexity and generalization performance. A smaller spread value results in a sharper RBF, leading to a more complex model and vice versa. The spread of radial basis functions is set to 500. As for model training, the data set used for training the RBFNN is the FOM data of the first 200 time steps.

2.3. Bubble Search Algorithm. Bubbles are generated in a BFB reactor when the superficial gas velocity exceeds the minimum fluidization velocity (U_{mf}) during gas−solid flow in a fluidized bed.[28] Currently, several studies have reported on the observation of mesoscopic characteristics of bubbles in a gas−solid flow. Tian et al.[29] pioneeringly proposed the density-based spatial clustering of applications with noise (DBSCAN) method

https://doi.org/10.1021/acs.iecr.3c03747
Ind. Eng. Chem. Res. 2024, 63, 1634−1648

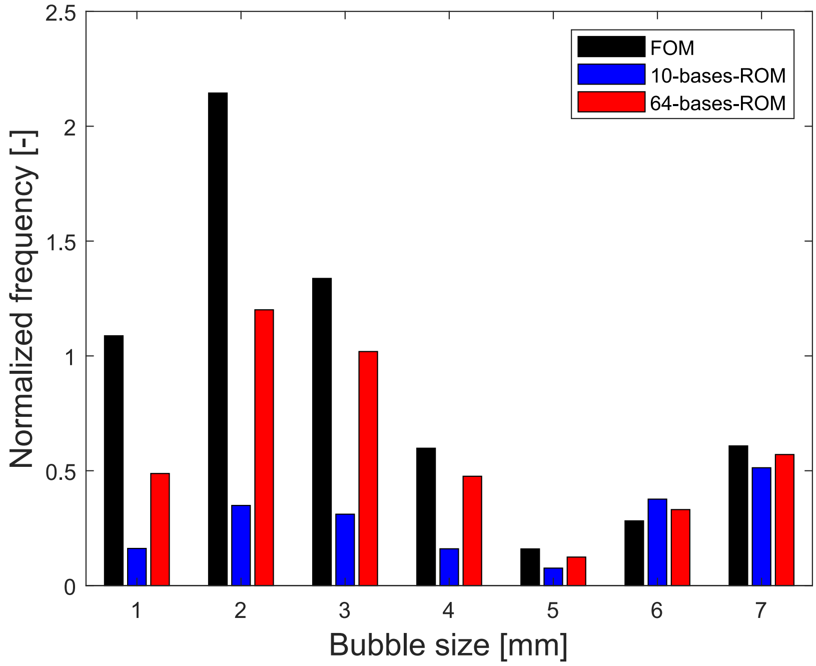

Figure 12. Comparison of the frequency for bubbles in case-1: FOM (TFM), 10-bases-ROM, 64-bases-ROM (single step).

for detecting particle clusters in particle−fluid systems. This method defines dense particle clusters based on different system structures, thereby requiring minimal manual intervention. Subsequently, the DBSCAN-based method was compared with the probe method and the Voronoi-based Method. It was found that both the DBSCAN-based method and the Voronoi-based method can provide additional information regarding cluster shape, topology, and other factors. The kinetic analysis of particle clusters using the Voronoi-based method allows for an in-depth exploration of the intrinsic mechanisms involved in the clustering process.[30] In the context of this work, our primary objective is to quantify the size and frequency of the bubbles for ROM validation purposes. Consequently, acquiring detailed information about the shape and internal mechanisms of bubbles (or particle clusters) by such newer and more sophisticated techniques is not deemed essential. Thus, the following simplified bubble search algorithm will be employed, as it sufficiently fulfills the validation requirements.

Bubble boundaries are identified as isosurfaces with a threshold voidage of 0.6−0.8.[31,32] In this work, a voidage of 0.8 is used as the critical voidage to identify the boundary of the bubble. Technically, a bubble can be represented by many neighboring cells with a voidage greater than a threshold. The bubble search algorithm process is shown in Figures 3 and 4; the main idea is as follows:

(1) The computing cells with voidage greater than 0.8 are retrieved in the search domain and are put into the vector $\mathbf{Cell_{bub}}$. The number of cells with voidage greater than 0.8 is counted, and the characteristics of the cell volume and voidage are recorded. As shown in Figure 3, the voidage of cells with specific tags 24, 33, 34, 43, 44, 53, 54, 63, 64, 74, and 84 reaches the threshold. The specific cells are put into the vector $\mathbf{Cell_{bub}}$ and searched.

(2) For any cell i in $\mathbf{Cell_{bub}}$: ① Create a vector $\mathbf{Bub}_i$ with cell i as the target cell. As shown in Figure 3, cell 54 is the target cell. ② Retrieve the neighborhood of cell i in $\mathbf{Cell_{bub}}$. If the voidage is greater than 0.8, put the neighborhood cells into the vector $\mathbf{Bub}_i$. Cells 43, 44, 53, 63, and 64 are put into vector $\mathbf{Bub}_i$. ③ Use the adjacent cells in the set $\mathbf{Bub}_i$ as the new starting cells and continue to search for the corresponding adjacent cells until the number of cells in the set no longer increases. In Figure 3, cells 33, 34, 74, 24, and 84 are successively incorporated into the vector $\mathbf{Bub}_i$. ④ Delete the repeated cells in the vector $\mathbf{Bub}_i$.

(3) Subsequent searches are performed on all cells in $\mathbf{Cell_{bub}}$, and if cell k is already contained in a bubble, the cell is skipped. If cell k is not included in the bubble, repeat step (2) until all cells of $\mathbf{Cell_{bub}}$ are traversed and bubble retrieval is completed.

Based on the bubble search algorithm, the bubble size is calculated as follows:[33]

$$d_b = 2 \times \sqrt[3]{3V_b/4\pi} \tag{15}$$

where V_b is the bubble volume, given by

$$V_b = \sum_{i=1}^{N_{cell}} V_{cell,i}\varepsilon_{cell,i} \tag{16}$$

where N_{cell} represents the total amount of cells contained in the bubble. $V_{cell,i}$ represents the volume of the ith cell. $\varepsilon_{cell,i}$ is the voidage of the ith cell. The central coordinate of the bubble is calculated by averaging the coordinates of all of the computational cells contained in the bubble:

$$C_b = \frac{1}{N_{cell}} \sum_{i=1}^{N_{cell}} C_{cell,i} \tag{17}$$

where C_b is the coordinate of the bubble. $C_{cell,i}$ is the coordinate of the ith cell.

The bubble search algorithm is verified with the experimental measurement by Laverman et al.[28,33] Figure 4 shows the comparison between predicted values and experimental data on the relationship between the bubble diameter and axial position at different inlet velocities. At three inlet velocities, the developed bubble detection algorithm can well capture the

https://doi.org/10.1021/acs.iecr.3c03747
Ind. Eng. Chem. Res. 2024, 63, 1634−1648

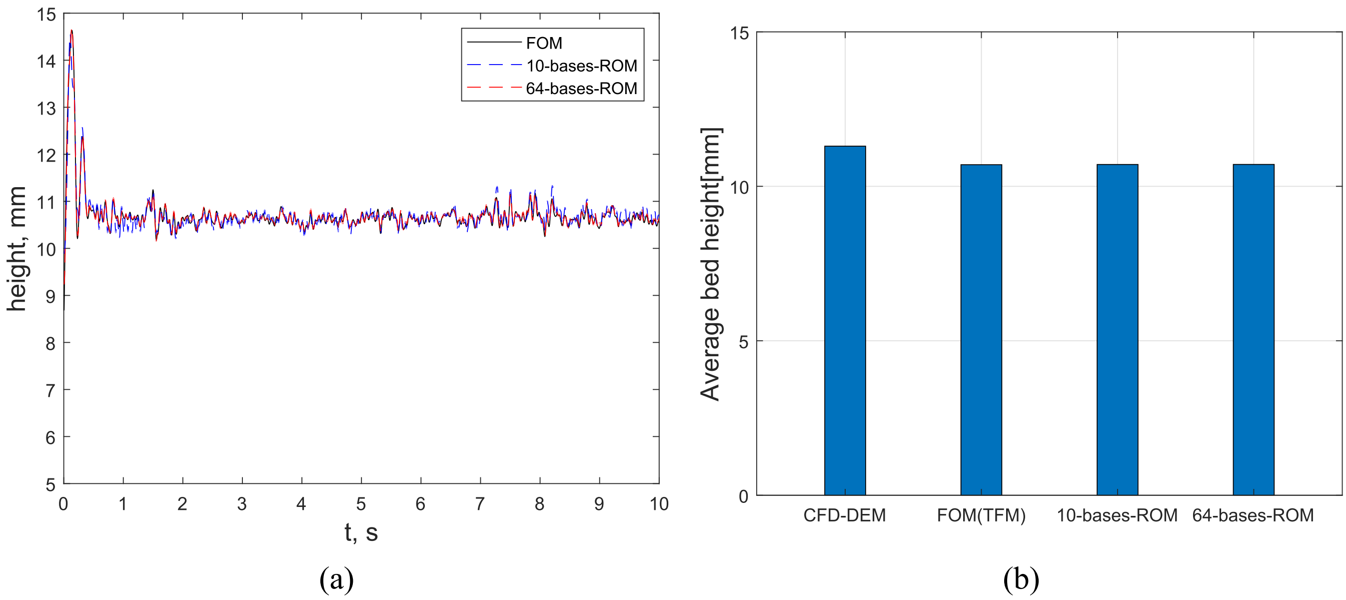

Figure 13. Time-evolution of bed expansion height and time-averaged bed expansion height in the BFB predicted by the FOM and single-step ROM in Case-2: (a) time-evolution bed expansion height; (b) time-averaged bed expansion height.

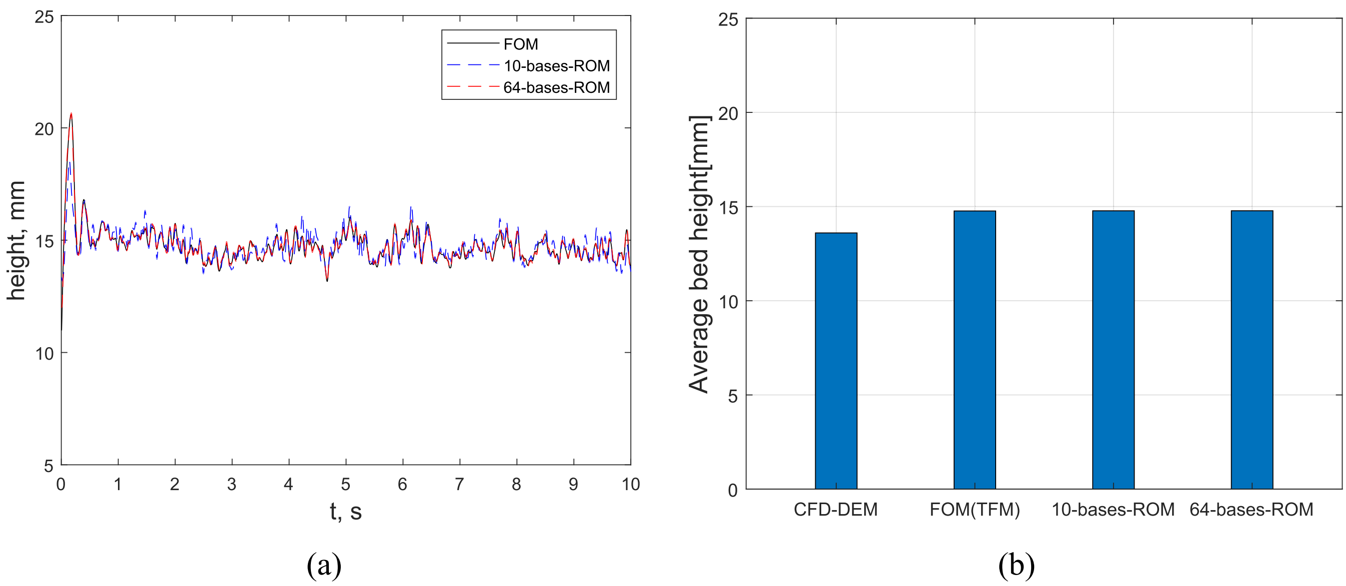

Figure 14. Time-evolution of bed expansion height and time-averaged bed expansion height in the BFB predicted by the FOM and single-step ROM in Case-3: (a) time-evolution bed expansion height; (b) time-averaged bed expansion height.

variation trend of bubble volume as a function of the height, indicating that the developed bubble search algorithm can accurately predict the bubble behaviors in the BFB.

In this paper, the bubble search algorithm is carried out on each snapshot to count the frequency of bubble emergence of each size in all snapshots rather than the frequency of bubble formation. When two bubbles overlap, fragment, and coalesce, the statistical accuracy of the ROM and FOM will be slightly affected, but the impact is insignificant. The bubble search algorithm uses a threshold voidage as a principle for bubble boundary determination, which will result in the inability to accurately analyze the dynamic process of actual bubble fragmentation and coalescence. However, in the context of statistics, when an appropriate threshold voidage is specified and the number of statistical bubbles is large enough, the error in the fragmentation and coalescence process of a single bubble can be neglected, and the statistical accuracy of bubble frequency will be insignificantly affected.

3. NUMERICAL SETTINGS

In this section, the ROM is validated regarding gas−solid flow dynamics in a BFB. The numerical settings in this work refer to the study from Li et al.[27] Figure 5 shows the schematic diagram of the BFB, which has dimensions of 20 mm × 5 mm × 50 mm. The computational domain is divided into 40 × 10 × 100 structured elements.

For the base case, the inlet velocity is set as 0.10 m/s, and the outlet pressure is specified as 101,325 Pa. The walls are all assigned with no-slip and constant temperature boundary conditions. The Syamlal and O'Brien drag force model[35] is employed. The time step was set to 5×10^{-4} s, and the physical time for each case is 10 s. The single snapshot time interval was 5

https://doi.org/10.1021/acs.iecr.3c03747
Ind. Eng. Chem. Res. 2024, 63, 1634−1648

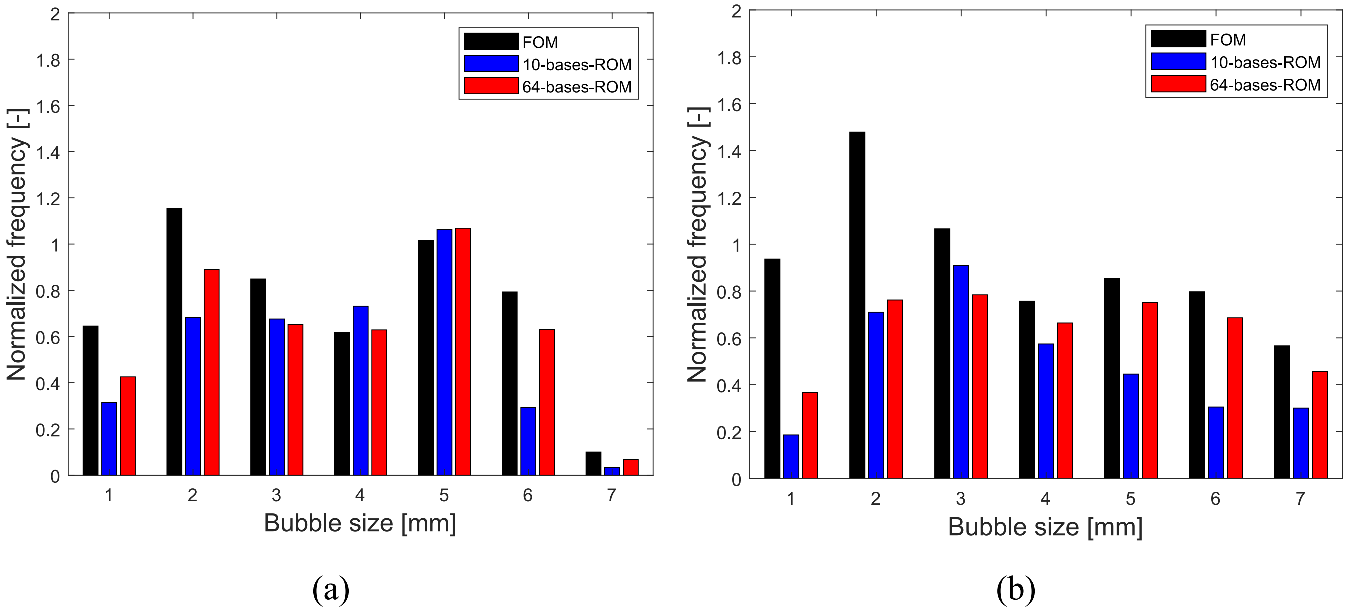

Figure 15. Comparison of the frequency for bubbles of different sizes, including FOM(TFM), 10-bases-ROM, and 64-bases-ROM (single step): (a) Case-2; (b) Case-3.

$\times 10^{-3}$ s, so 2000 snapshots were obtained. Depending on the number k of POD bases chosen, a matrix of ($k \times 2000$) ROM coefficients can be obtained. The detailed numerical settings are given in Table 1. Table 2 shows the different cases studied in the present work.

The thermophysical properties of particles are given in Table 3 and are consistent with the experiment. The viscosity and density of the gas are 1.8×10^{-5} Pa·s and 1.0 kg/m^3, respectively. The density and size of the particle are 2.5×10^3 kg/m^3 and 0.16 mm, respectively.

4. RESULTS AND DISCUSSION

4.1. POD Analysis. Figure 6 shows the time-averaged solid holdup in the central slice of the BFB ($z = 0$) of the base case (Case-1) obtained from the FOM results. It can be seen that the particles are mainly concentrated in the lower part of the bed with a clear demarcation line from the freeboard. Figure 7 shows the main mode diagrams after the flow field is decomposed, from the first order to the eighth order. The solid holdup values of the POD spatial modes are relative values, which appear fuzzy due to the simple and regular characteristics of the modes. The first-order mode is the most dominant mode of the flow field, and the number of features contained decreases with the order.

Figure 8a shows the proportion of each mode's energy to the total energy at different orders of the base case. It can be seen that the first-order mode contains the most features, accounting for about 10.8%. As the order increases, the number of features contained in each mode decreases step by step. After the 24th order mode, the number of features contained in each mode is less than 1%. The cumulative energy content of the first k modes at different orders is shown in Figure 8b. According to the desired accuracy, the first k modes are selected for superposition to better reduce the flow process in the BFB. As indicated in eq 6, different orders can be selected according to different accuracy requirements. When the accuracy requirements are 0.5 and 0.9, respectively, the orders can be chosen as 10 and 64, respectively. Figure 9 shows the time-evolution profiles of the coefficients of the first 10 orders of modalities. The distribution of the solid holdup in the BFB can be fully demonstrated by combining each mode with the corresponding coefficient at any given moment. In this way, the flow field in the BFB can be obtained.

Figure 10 shows the reproduction of the solid holdup in the BFB of the FOM, 10-bases-ROM, 35-bases-ROM, and 64-bases-ROM at different time instants. It is noted that the 10-bases-ROM is unable to accurately reproduce the solid holdup distribution in the BFB, where many details are omitted. As the number of orders increases, a more accurate flow field can be achieved. For the modes with the inclusion of 64 orders, the ROM can reproduce the flow field. Although the 10-bases-ROM may not yield entirely accurate predictions of the flow field, its high efficiency still holds significant industrial value. A comparison with the 64-bases-ROM makes the difference in accuracy resulting from varying orders more intuitive. Based on the above results, the representative modes with the first 10 orders and the first 64 orders are used to construct the ROM of the BFB and to compare the specific effect of the number of orders on the reconstruction accuracy in the subsequent sections.

4.2. ROM Model Validation at Different Basis Numbers. Figure 11 shows the bed expansion height in the BFB predicted by the FOM and single-step ROM at different orders in the base case (Case-1). The TFM results in this work are compared with the CFD-DEM results from Li et al.[27] to further prove the accuracy of ROM. The first 10 modes and the first 64 modes are selected in the ROM. Both the 10-bases-ROM and the 64-bases-ROM can reproduce the bed expansion height in the BFB, and the 64-bases-ROM has a better performance than the 10-bases-ROM.

Figure 12 shows the frequency statistics for bubbles in the BFB. The trend dependence of the frequency on bubble size is a feature of the FOM, and the ROM is used to reconstruct this feature. The 10-bases-ROM only retains 50% of the features of the FOM, and the size of bubbles is based on the threshold voidage. The voidage of the grid loses half of the features, making it more difficult to determine the threshold grid of the boundary. Hence, employing the 10-bases-ROM for quantifying bubble frequency characteristics not only diminishes the bubble

https://doi.org/10.1021/acs.iecr.3c03747
Ind. Eng. Chem. Res. 2024, 63, 1634−1648

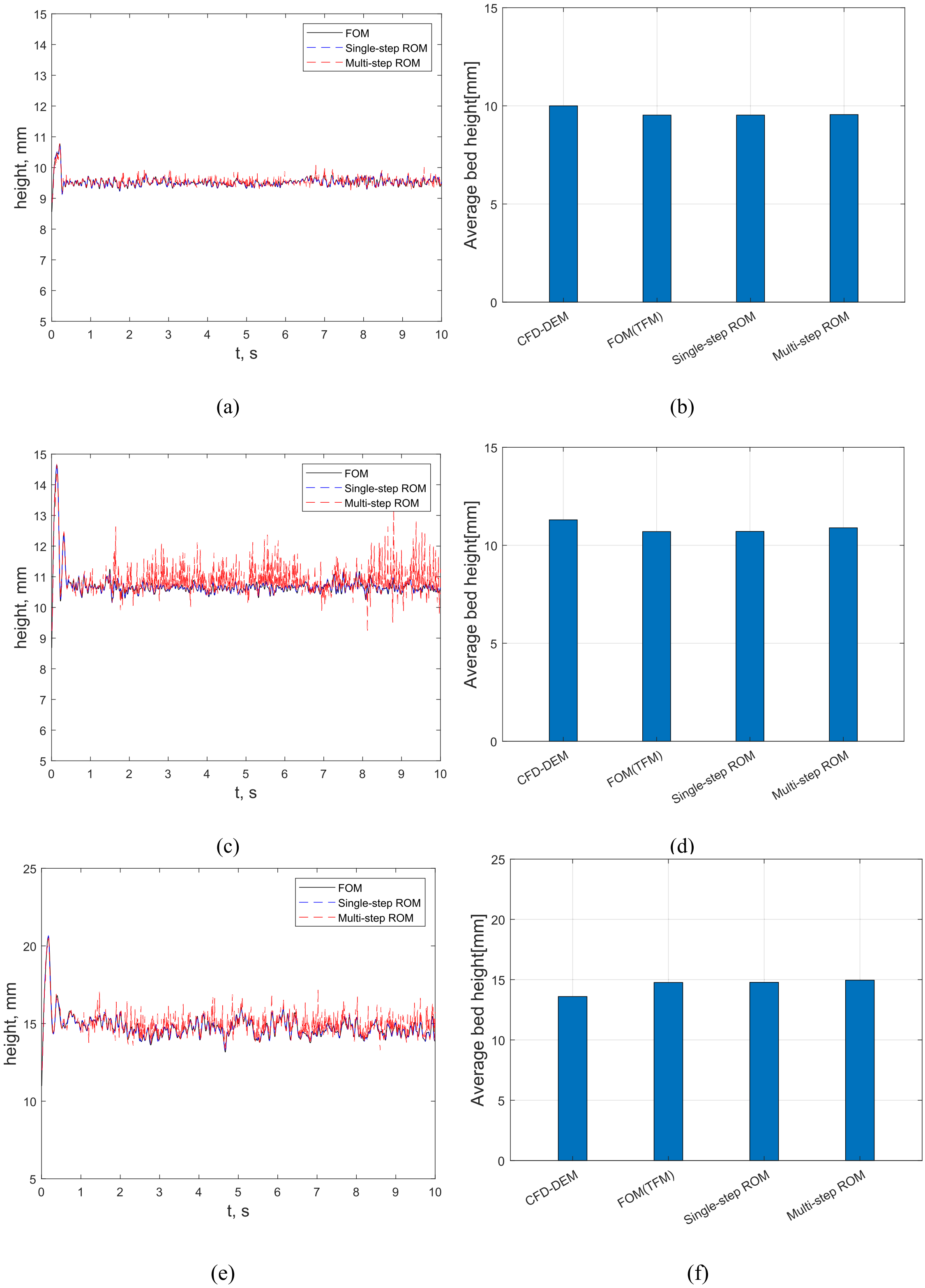

Figure 16. Bed expansion height in the BFB predicted by the FOM, single-step ROM, and multistep ROM: (a) Case-1: time-evolution bed expansion height; (b) Case-1: time-averaged bed expansion height; (c) Case-2: time-evolution bed expansion height; (d) Case-2: time-averaged bed expansion height; (e) Case-3: time-evolution bed expansion height; (f) Case-3: time-averaged bed expansion height.

frequency for each size but may also disrupt the trend dependence of the predicted frequency on bubble size. This error is to be expected. The 64-bases-ROM retains more features, so trend dependence will be retained with a greater probability. Compared with the FOM, the 10-bases-ROM differs by an average value of 60%, and the 64-bases-ROM differs by an average value of 27% for the frequency of all sizes of bubbles. The difference between the 10-bases-ROM and the 64-bases-ROM for the frequency of all sizes of bubbles is 48%. The statistical difference between the FOM and ROM for smaller

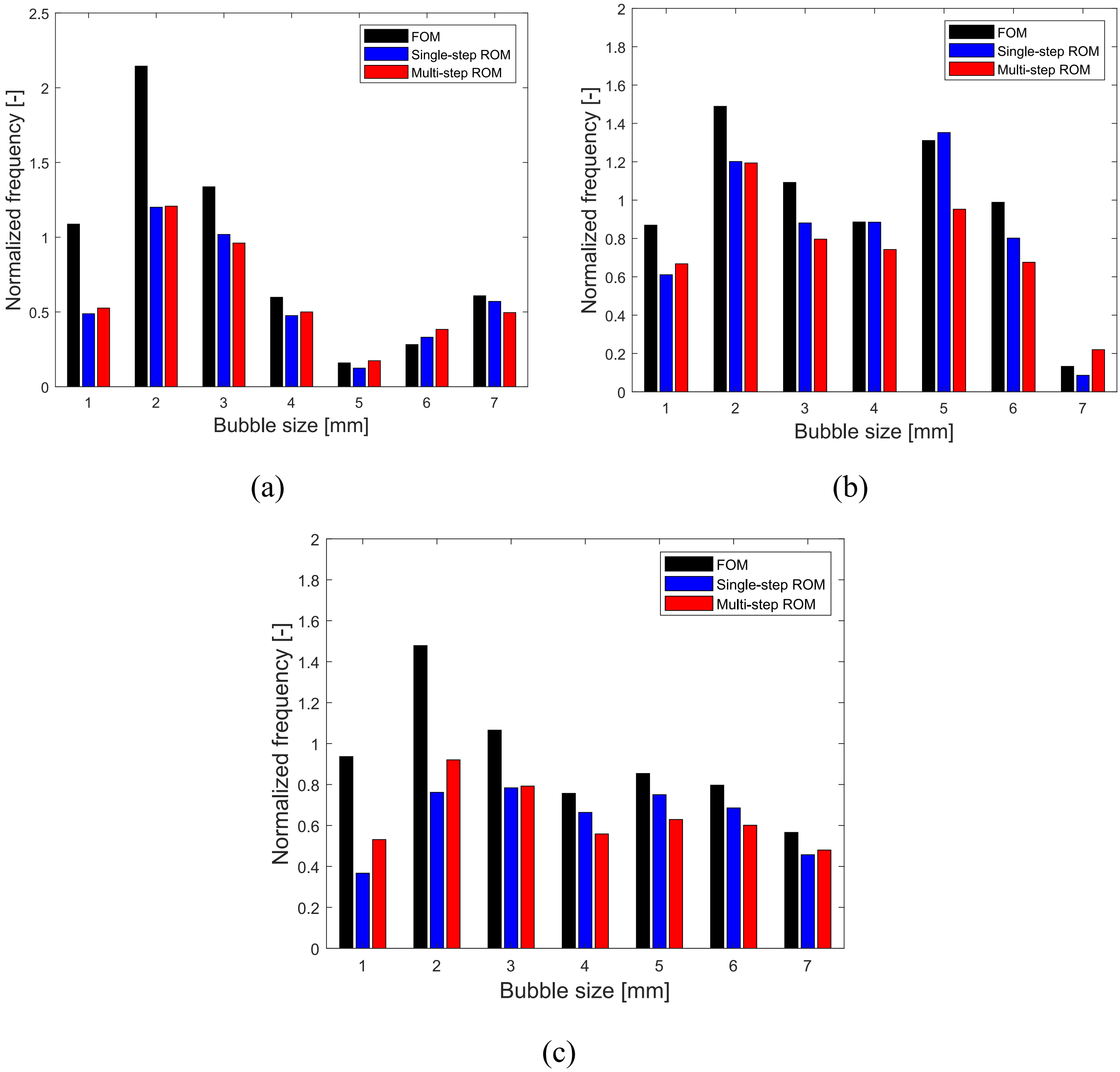

Figure 17. Comparison of the frequency for bubbles of different sizes (FOM (TFM), ROM (single step), ROM (multistep)): (a) Case-1; (b) Case-2; (c) Case-3.

Table 4. Time Consumption of the POD

case	case-1	case-2	case-3
POD [s]	29.9	33.2	35.9

bubbles may be due to the neglect of some details in ROM, making it difficult to capture tiny bubble structures. As the bubble size increases, the difference between the FOM and ROM gradually decreases, and the ROM has a better performance in flow field reconstruction. Based on the above results, a low-order ROM (10-bases-ROM) has a worse performance on the flow field reconstruction, which has a greater difference from FOM's prediction results. In contrast, the high-order ROM (64-bases-ROM) has a better performance on the reconstruction of the flow field, which is in line with FOM's prediction results.

Table 5. Time Consumption of the FOM and ROM

condition	model	CFD/prediction [s]	reduction
case-1	FOM	34.7	
	ROM-10	0.048	723
	ROM-64	0.269	129
case-2	FOM	35.6	
	ROM-10	0.056	635
	ROM-64	0.295	121
case-3	FOM	34.0	
	ROM-10	0.046	739
	ROM-64	0.262	130

Figures 13 and 14 show the bed expansion heights in the BFB for different cases (Case-2 and Case-3). Similar to Case-1, the 64-bases-ROM has a better performance than the 10-bases-

https://doi.org/10.1021/acs.iecr.3c03747
Ind. Eng. Chem. Res. 2024, 63, 1634−1648

ROM in Case-2 and Case-3, demonstrating the applicability of the ROM and the ability to complete the reduced order for simulation results under different operating conditions.

Figure 15 shows the frequency statistics of bubbles in the BFB for different cases (Case-2 and Case-3). It is noted that there is a small difference between the FOM and the ROM with different numbers of modes in the bubble distribution for Case-2 than for Case-1 and Case-3 (as shown in Figures 12 and 15b), which shows that the ROM's spatial characteristics of the working condition of Case-2 are easier to grasp. This is because compared with Case-1 (inlet gas velocity: initial bed inventory = 0.1 m/s: 2.145 g) and Case-3 (inlet gas velocity: initial bed inventory = 0.18 m/s: 2.681 g), Case-2 has a higher ratio of inlet gas velocity to initial bed inventory (inlet gas velocity: initial bed inventory = 0.18 m/s: 2.145 g), which leads to a more vigorous bubble movement, with less spatial detail being lost in all sizes of bubbles in the ROM. Therefore, the ROM in Case-2 has a better accuracy performance than in Case-1 and Case-3.

4.3. ROM Model Validation at Different Prediction Steps. Figure 16 shows the bed expansion height in the BFB for the FOM, single-step ROM, and multistep ROM in Case-1, Case-2, and Case-3. The order number of the ROM is chosen as 64, and the prediction steps are chosen as 1 and 5. It can be seen that the fluctuation of transient bed expansion height predicted by multistep ROM and FOM are within the same fluctuation range, and the time-averaged bed expansion heights predicted by both single-step ROM and multistep ROM maintain a high accuracy compared with the FOM. In Case-2, the difference in the fluctuation characteristics of the multistep ROM and FOM is relatively more obvious, which indicates that the multistep ROM's accuracy decreases when the flow field is more intense.

Figure 17 shows the frequency statistics for bubbles in the BFB for the single-step ROM and the multistep ROM (Case-1, Case-2, and Case-3). It is noted that there is a bigger difference between the multistep ROM and the single-step ROM in the bubble distribution for Case-2 than for Case-1 and Case-3, which shows that the ROM's temporal characteristics of the working condition of Case-2 are more difficult to grasp. This is because, compared with Case-1 (inlet gas velocity: initial bed inventory = 0.1 m/s: 2.145 g) and Case-3 (inlet gas velocity: initial bed inventory = 0.18 m/s: 2.681 g), Case-2 has a higher ratio of inlet gas velocity to initial bed inventory (inlet gas velocity: initial bed inventory = 0.18 m/s: 2.145 g), which leads to a more vigorous bubble movement, with bubble temporal characteristics captured more difficult in the multistep prediction. Since the change of bubbles is relatively not drastic in Case-1 and Case-3, the characteristics of time coefficients are easier to grasp. Therefore, the ROM in Case-1 and Case-3 has better stability than in Case-2.

4.4. Comparison of Model Accuracy and Computational Efficiency. ROM-10 represents 10-bases-ROM and ROM-64 represents 64-bases-ROM. The simulation cases run with a single core (12th Gen Intel(R) Core (TM) i7-12700H, 2.30 GHz). The ROM includes two steps: projection and prediction. However, the projection process is performed before prediction; therefore, it is not included in the ROM calculation time. Table 4 shows the consumption time of the POD. Table 5 shows the time consumption of the FOM and single-step ROM under different reduced basis numbers. The reduction is the ratio of FOM (CFD) single-step calculation time to ROM single-step calculation time. Among the three cases, the calculation efficiency of the 64-bases-ROM increases by about 120 times, and the calculation efficiency of the 10-bases-ROM increases by about 700 times as compared with the FOM.

5. CONCLUSIONS AND FUTURE DEVELOPMENTS

In this study, a ROM is constructed by using the POD/RBFNN coupling approach to obtain the main flow modes of the BFB and to make real-time predictions of some key parameters in the BFB, such as bed expansion height and bubble distribution. The ROMs are validated by comparing the predicted results with the FOM. In addition, the superiority of the ROM in terms of computational efficiency is demonstrated through a comparison of the computational times. The conclusions are as follows:

(1) The ROM constructed by POD/RBFNN can reduce the dimensionality of high-dimensional data, accurately reproduce the internal flow fields within the BFB, preserve the flow-related structures and modes that dominate the fluid dynamics, and improve the physical interpretability of the model.

(2) The 10-bases-ROM and 64-bases-ROM contain 50 and 90% of the energy, respectively. From the time-averaged and instantaneous results of bed expansion height, the results of different order reductions are in good agreement with the results of the FOM. In terms of bubble distribution, the 64-bases-ROM is more accurate than the 10-bases-ROM due to more detail contained in higher orders.

(3) As the ratio of inlet gas velocity to initial bed inventory increases, it is easier to grasp the spatial modes of the BFB flow field, but it is more difficult to predict the time coefficients.

(4) The calculation speed of the 64-bases-ROM is approximately 120 times that of the FOM, and the calculation speed of the 10-bases-ROM is approximately 700 times that of the FOM.

In future research, data assimilation and compressed sensing methods can be combined to complete the digital twin. In large-scale sensor networks, compressed sensing is used to reduce the transmission volume of the sensor nodes. The data assimilation technology is used to combine the compressed observation data with model data. Both of the above are finally integrated into a ROM to predict the system status accurately and efficiently.

■ ASSOCIATED CONTENT

Supporting Information

The Supporting Information is available free of charge at https://pubs.acs.org/doi/10.1021/acs.iecr.3c03747.

Main equations of the CFD-DEM method (Table S1); main equations of the TFM method (Table S2) (PDF)

■ AUTHOR INFORMATION

Corresponding Author

Kun Luo − *State Key Laboratory of Clean Energy Utilization, Zhejiang University, Hangzhou 310027, China; Shanghai Institute for Advanced Study of Zhejiang University, Shanghai 200120, China;* orcid.org/0000-0003-3644-9400; Email: zjulk@zju.edu.cn

Authors

Xiaofei Li − *State Key Laboratory of Clean Energy Utilization, Zhejiang University, Hangzhou 310027, China*

Shuai Wang − *State Key Laboratory of Clean Energy Utilization, Zhejiang University, Hangzhou 310027, China*

Dali Kong − *State Key Laboratory of Clean Energy Utilization, Zhejiang University, Hangzhou 310027, China*
Jianren Fan − *State Key Laboratory of Clean Energy Utilization, Zhejiang University, Hangzhou 310027, China; Shanghai Institute for Advanced Study of Zhejiang University, Shanghai 200120, China;* orcid.org/0000-0002-6332-6441

Complete contact information is available at:
https://pubs.acs.org/10.1021/acs.iecr.3c03747

Notes

The authors declare no competing financial interest.

■ ACKNOWLEDGMENTS

The present work was supported by the National Natural Science Foundation of China (No. 51925603) and the Fundamental Research Funds for the Central Universities (No. 2022ZFJH004), which should be sincerely acknowledged.

■ REFERENCES

(1) Basu, P. *Circulating Fluidized Bed Boilers: Design, Operation and Maintenance*; Springer International Publishing: Cham, 2015.
(2) Wang, S.; Luo, K.; Hu, C.; et al. Particle-Scale Investigation of Heat Transfer and Erosion Characteristics in a Three-Dimensional Circulating Fluidized Bed. *Ind. Eng. Chem. Res.* **2018**, *57* (19), 6774−6789.
(3) Zhong, W.; Yu, A.; Zhou, G.; et al. CFD simulation of dense particulate reaction system: Approaches, recent advances and applications. *Chem. Eng. Sci.* **2016**, *140*, 16−43.
(4) Wang, S.; Luo, K.; Hu, C.; et al. CFD-DEM simulation of heat transfer in fluidized beds: Model verification, validation, and application. *Chem. Eng. Sci.* **2019**, *197*, 280−295.
(5) Wang, S.; Luo, K.; Hu, C.; et al. CFD-DEM study of the effect of ring baffles on system performance of a full-loop circulating fluidized bed. *Chem. Eng. Sci.* **2019**, *196*, 130−144.
(6) Patil, A. V.; Peters, E. A. J. F.; Kuipers, J. A. M. Comparison of CFD−DEM heat transfer simulations with infrared/visual measurements. *Chem. Eng. J.* **2015**, *277*, 388−401.
(7) Aversano, G.; D'Alessio, G.; Coussement, A.; et al. Combination of polynomial chaos and Kriging for reduced-order model of reacting flow applications. *Results Eng.* **2021**, *10*, No. 100223.
(8) Sun, L.; Gao, H.; Pan, S.; et al. Surrogate modeling for fluid flows based on physics-constrained deep learning without simulation data. *Comput. Methods Appl. Mech. Eng.* **2020**, *361*, No. 112732.
(9) Aversano, G.; Bellemans, A.; Li, Z.; et al. Application of reduced-order models based on PCA & Kriging for the development of digital twins of reacting flow applications. *Comput. Chem. Eng.* **2019**, *121*, 422−441.
(10) Aversano, G.; Ferrarotti, M.; Parente, A. Digital twin of a combustion furnace operating in flameless conditions: reduced-order model development from CFD simulations. *Proc. Combust. Inst.* **2021**, *38* (4), 5373−5381.
(11) Li, S.; Duan, G.; Sakai, M. On POD-based modal analysis in simulations of granular flows. *Powder Technol.* **2023**, *413*, No. 118058.
(12) Sun, F.; Su, W. Y.; Wang, M. Y.; et al. RBF-POD reduced-order modeling of flow field in the curved shock compression inlet. *Acta Astronaut.* **2021**, *185*, 25−36.
(13) Ding, S.; Yang, R. Reduced-order modelling of urban wind environment and gaseous pollutants dispersion in an urban-scale street canyon. *J. Saf. Sci. Resil.* **2021**, *2* (4), 238−245.
(14) Zhu, L. T.; Chen, X. Z.; Ouyang, B.; et al. Review of Machine Learning for Hydrodynamics, Transport, and Reactions in Multiphase Flows and Reactors. *Ind. Eng. Chem. Res.* **2022**, *61* (28), 9901−9949.
(15) Han, D.; Yu, B.; Yu, G.; et al. Study on a BFC-based POD-Galerkin ROM for the steady-state heat transfer problem. *Int. J. Heat Mass Transfer* **2014**, *69*, 1−5.
(16) Zhu, L.; Ouyang, B.; Lei, H.; et al. Conventional and data-driven modeling of filtered drag, heat transfer, and reaction rate in gas-particle flows. *AIChE J.* **2021**, *67* (8), No. e17299.
(17) Zhu, L.; Tang, J.; Luo, Z. Machine learning to assist filtered two-fluid model development for dense gas-particle flows. *AIChE J.* **2020**, *66* (6), No. e16973.
(18) Ostrowski, Z.; Białecki, R. A.; Kassab, A. J. Solving inverse heat conduction problems using trained POD-RBF network inverse method. *Inverse Probl. Sci. Eng.* **2008**, *16* (1), 39−54.
(19) Chen, X.; Liu, L.; Long, T.; et al. A reduced order aerothermodynamic modeling framework for hypersonic vehicles based on surrogate and POD. *Chin. J. Aeronaut.* **2015**, *28* (5), 1328−1342.
(20) Huayamave, V.; Ceballos, A.; Barriento, C.; et al. RBF-trained POD-accelerated CFD analysis of wind loads on PV systems. *Int. J. Numer. Methods Heat Fluid Flow* **2017**, *27* (3), 660−673.
(21) Kadeethum, T.; Ballarin, F.; Choi, Y.; et al. Non-intrusive reduced order modeling of natural convection in porous media using convolutional autoencoders: Comparison with linear subspace techniques. *Adv. Water Resour.* **2022**, *160*, No. 104098.
(22) Huang, R.; Mahvi, A.; Odukomaiya, W.; et al. Reduced-order modeling method for phase-change thermal energy storage heat exchangers. *Energy Convers. Manage.* **2022**, *263*, No. 115692.
(23) Margheri, L.; Sagaut, P. A hybrid anchored-ANOVA-POD/Kriging method for uncertainty quantification in unsteady high-fidelity CFD simulations. *J. Comput. Phys.* **2016**, *324*, 137−173.
(24) Ahmed, S. E.; Rahman, S. M.; San, O.; et al. Memory embedded non-intrusive reduced order modeling of non-ergodic flows. *Phys. Fluids* **2019**, *31* (12), No. 126602.
(25) Lu, Q.; Wang, L.; Li, L. Efficient uncertainty quantification of stochastic problems in CFD by combination of compressed sensing and POD-Kriging. *Comput. Methods Appl. Mech. Eng.* **2022**, *396*, No. 115118.
(26) Lee, W.; Jang, K.; Han, W.; et al. Model order reduction by proper orthogonal decomposition for a 500 MWe tangentially fired pulverized coal boiler. *Case Stud. Therm. Eng.* **2021**, *28*, No. 101414.
(27) Li, S.; Duan, G.; Sakai, M. Development of a reduced-order model for large-scale Eulerian−Lagrangian simulations. *Adv. Powder Technol.* **2022**, *33* (8), No. 103632.
(28) Kong, D.; Wang, S.; Luo, K.; et al. Bubble dynamics and thermochemical characteristics of bubbling fluidized bed methanation. *Fuel* **2023**, *338*, No. 127292.
(29) Tian, T. Detecting Particle Clusters in Particle-Fluid Systems by a Density Based Method. *Commun. Comput. Phys.* **2019**, *26* (5), 1617−1630.
(30) Kong, L.; Xu, J.; Wang, J.; et al. Characterizing Particle Clustering Behavior in Dense Gas−Solid Suspensions. *Ind. Eng. Chem. Res.* **2023**, *62*, 19145−19160.
(31) Lu, L.; Konan, A.; Benyahia, S. Influence of grid resolution, parcel size and drag models on bubbling fluidized bed simulation. *Chem. Eng. J.* **2017**, *326*, 627−639.
(32) Li, T.; Dietiker, J. F.; Zhang, Y.; et al. Cartesian grid simulations of bubbling fluidized beds with a horizontal tube bundle. *Chem. Eng. Sci.* **2011**, *66* (23), 6220−6231.
(33) Laverman, J. A.; Roghair, I.; van Annaland, M. S.; et al. Investigation into the hydrodynamics of gas−solid fluidized beds using particle image velocimetry coupled with digital image analysis. *Can. J. Chem. Eng.* **2008**, *86* (3), 523−535.
(34) Kong, D.; Wang, S.; Luo, K.; et al. Numerical study of biomass gasification combined with CO_2 absorption in a bubbling fluidized bed. *AIChE J.* **2023**, *69* (8), No. e18096.
(35) Syamlal, M.; O'Brien, T. J. *The Derivation of a Drag Coefficient Formula from Velocity Voidage Correlations*; US Department of energy, Office of Fossil Energy, NETL: Morgantown, WV, 1987.